ACS APPLIED MATERIALS & INTERFACES

www.acsami.org

Research Article

Multifunctional Mg−C Bilayer Interphase for Anode-Free Solid-State Batteries

Ruixin Wu, Sufu Liu, Ruihao Deng, Ru Xiao, Keng Xu, Chengyin Fu,* Andrea Ingenito, and Fudong Han*

Cite This: https://doi.org/10.1021/acsami.6c01094

Read Online

ACCESS | Metrics & More | Article Recommendations | Supporting Information

ABSTRACT: The development of anode-free solid-state batteries can significantly improve the energy density of today's lithium-ion batteries, but it has proven difficult due to challenges in regulating Li deposition/dissolution. Here, we report a Mg/C bilayer interphase for anode-free batteries. We observed the lithiation of both Mg and C prior to the initial plating process. Moreover, a larger nucleation overpotential can be observed on lithiated carbon (Li−C) than on lithiated magnesium (Li−Mg). As a result, instead of plating at the interface between Li−C and the solid electrolyte (SE), Li will penetrate through the Li−C and the plate at the interface between Li−C and Li−Mg. The regulated Li plating was also validated through cross-sectional scanning electron microscopy images. As a result, a uniform Li plating and stripping can be achieved underneath the Li−C. The effective separation of the SE and the plated Li enabled stable plating/stripping cycles at an areal capacity of 2 mAh/cm^2 at room temperature with an average Coulombic efficiency of >99%. The results provide important insights into understanding and designing interlayers for anode-free solid-state batteries.

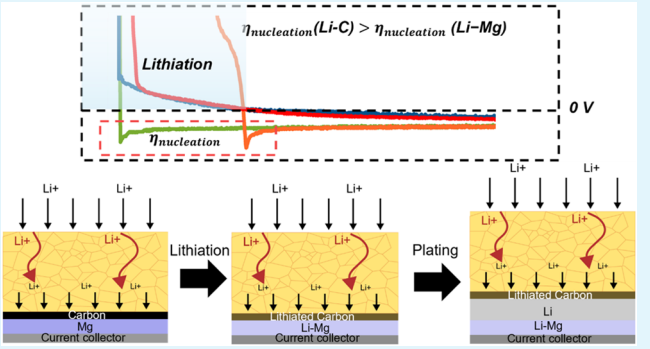

KEYWORDS: *anode-free, solid-state batteries, sulfide electrolyte, interlayer design, Mg/C bilayer*

INTRODUCTION

Lithium metal anodes are considered the ultimate solution for high-energy batteries because of their high theoretical capacity (3860 mAh/g) and low electrode potential.[1,2] Among all lithium metal batteries, the anode-free concept, where only a current collector is used as the anode, and all lithium is from the cathode, can deliver the highest gravimetric and volumetric energy density due to high utilization of Li.[3] While extensive research has been done to use Li metal anodes in liquid-electrolyte batteries with great progress,[2,4,5] enabling anode-free concept with liquid electrolytes has proven challenging due to the loss of lithium inventory through the side reactions with the liquid electrolytes.[6−8] Solid electrolytes (SEs) have been considered a potential approach for anode-free batteries in recent years.[9,10] Although most SEs are not thermodynamically stable with Li,[11] the formation of solid electrolyte interphase (SEI) in solid-state batteries is less dynamic than in the liquid-electrolyte cells because the noninfiltrative feature of solids eliminates the process of reforming part of SEI upon cracking/fracture.[12] As a matter of fact, the only anode-free battery that can cycle for thousands of cycles at a higher current density (>5 mA/cm^2) at room temperature is achieved in solid-state thin-film batteries based on LiPON electrolyte.[13] However, transferring the success from LiPON-based thin-film batteries to high-energy, bulk-type, solid-state anode-free batteries based on superionic SEs such as thiophosphates has been challenging due to the limited electrochemical stability of SEs against Li,[14] dendrite growth during plating,[15−17] and void formation at the Li/electrolyte interface during stripping.[18−20]

Various interlayer concepts using alloy- and ceramic-based materials have been developed to address these challenges for realizing bulk-type solid-state anode-free batteries. While the alloy-based interlayer can help improve the homogeneity of plating/stripping by enhancing interfacial contact due to the migration of alloy elements into bulk Li, it is questionable whether the effect can be sustained after long-term plating/stripping cycles.[21,22] Moreover, the utilization of an alloy-based interlayer alone cannot prevent the direct contact between plated Li and SE, and thus, dendrites can still form and penetrate through the SE layer. The utilization of a ceramic interlayer such as $LiBH_4$−LiI[23] can help suppress the side reactions between SEs and Li, thus increasing the plating/stripping efficiency. However, this ceramic interlayer is not

Received: January 16, 2026
Revised: February 22, 2026
Accepted: February 25, 2026

Downloaded via RENSSELAER POLYTECHNIC INST on March 4, 2026 at 13:31:31 (UTC).
See https://pubs.acs.org/sharingguidelines for options on how to legitimately share published articles.

© XXXX The Authors. Published by American Chemical Society

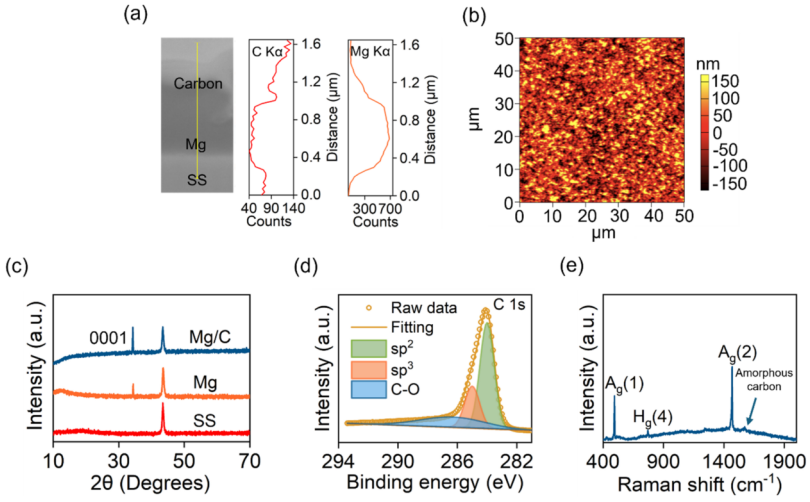

Figure 1. (a) Cross-sectional FIB/SEM image and EDS line scan result of the Mg/C bilayer on the stainless-steel current collector; (b) AFM altitude of Mg/C bilayer; (c) XRD patterns of Mg/C, Mg, and stainless-steel current collector; (d) high-resolution C 1s XPS spectra of Mg/C bilayer; and (e) Raman spectrum of Mg/C bilayer.

effective in suppressing dendrite formation.[23] A milestone work on the interlayer design was reported by Samsung.[24] The team reported a 5 μm-thick nanocomposite interlayer, consisting of Ag nanoparticles and carbon black, which can effectively regulate Li deposition in a solid-state cell based on Li_6PS_5Cl SE. The authors reported that during initial plating, Ag will migrate and direct the plating of Li at the Ag/C interface (underneath carbon) rather than at the carbon/SE interface (above carbon), thus separating the plated Li from the SE by carbon. The utilization of this interlayer enabled an anode-free solid-state battery with a high energy density of >900 Wh/L, a stable Coulombic efficiency of >99.4%, and a long cycle life of 1000 times,[24] despite by mechanism that remains elusive. A fundamental question would be why the Li was plated at the carbon/Ag interface rather than the carbon/SE interface, given the large electronic conductivity of the Ag−C interlayer.[25]

Stimulated by the impressive performance, several studies have been reported to understand the mechanism of the Ag−C interlayer. Suzuki et al. reported that the regulation of Li plating underneath carbon cannot be achieved after replacing carbon black with graphite in the Ag−C interlayer.[26] Instead, Li is plated on top of graphite, leading to a quick shorting of the cell. The same team also reported the effect of metals such as Zn, Sn, and Al in the metal−carbon black interlayer on the behavior of plating and stripping, and only Zn was reported to exhibit the same effect of Ag, although the solubility and mobility of Zn in Li is much smaller than Ag,[27] and both Sn-carbon black and Al-carbon black interlayer will lead to Li plating at the carbon/SE interface. The result suggests that both carbon and metal play important roles in regulating Li plating. By studying the effect of particle size of carbon in the interlayer, Lee et al. demonstrated that the utilization of smaller carbon particles can lead to a better separation between the plated Li and SE, while partial or complete contact between plated Li and SE can be observed for the interlayer with large carbon particles.[28] Assuming that the electronic conductivity of the carbon does not change with particle size, the authors attributed the different plating behavior to the difference in the pore size of the carbon layer. The pore-size-dependent Li plating behavior also enabled the authors to propose that the transport of Li through the carbon interlayer is through diffusional creep (also known as Coble creep[29]) of Li metal, rather than Li ions.[28] Based on the same concept, the team also developed a three-dimensional (3D) host with carbon black on top and stacked Ni nanoparticles at the bottom to facilitate the creep of Li.[30] A recent work from Fan et al. reported that Li plating at the carbon black/SE interface can occur if there is no Ag in the interlayer.[31] Tu et al. recently reported that the performance of Ag−C interlayer strongly depends on the assembly pressure of the solid-state cell, introducing a critical role of interfacial adhesion, which is beyond the material properties of the interlayer, in regulating Li plating.[32] A follow-up work from Tu and co-workers further proposed that the preferred Li deposition at the C/SE interface is due to its higher interfacial resistance than the Ag/C interface.[33] A most recent work from Dasgupta et al. quantifies the effect of interfacial adhesion using cells laminated at different pressures and demonstrated an interfacial-toughness-dependent deposition behavior for the same hard carbon interlayer. Specifically, they revealed that Li was plated underneath the carbon with a high interfacial toughness and above the carbon with a low interfacial toughness.[34] While Sn-carbon black interlayer did not help regulate Li plating underneath carbon from Suzuki et al's work,[26] a recent work from Kim et al. did observe the effective separation of Li and SE through a Sn-carbon interlayer.[35] The work mentioned above provided critical insights to understand the mechanism of the metal-C interlayer. However, large inconsistencies exist in literature results, and sharply different results have been reported for interlayers with the same metal (e.g., Sn)[26,35] or the same metal-C interlayer under different mechanical conditions.[34] The findings suggest that the resultant performance of the interlayer is not just a function of material properties but also related to interfacial mechanics. However, there is still no unifying theory that can reconcile all of the experimental results, and knowledge gaps remain to understand the exact mechanisms of metal−carbon interlayers to establish their design principles.

Herein, we report a Mg−C bilayer for anode-free solid-state batteries. The rationale behind the design is that if Ag and C in the nanocomposite layer have to separate during Li plating,

https://doi.org/10.1021/acsami.6c01094
ACS Appl. Mater. Interfaces XXXX, XXX, XXX−XXX

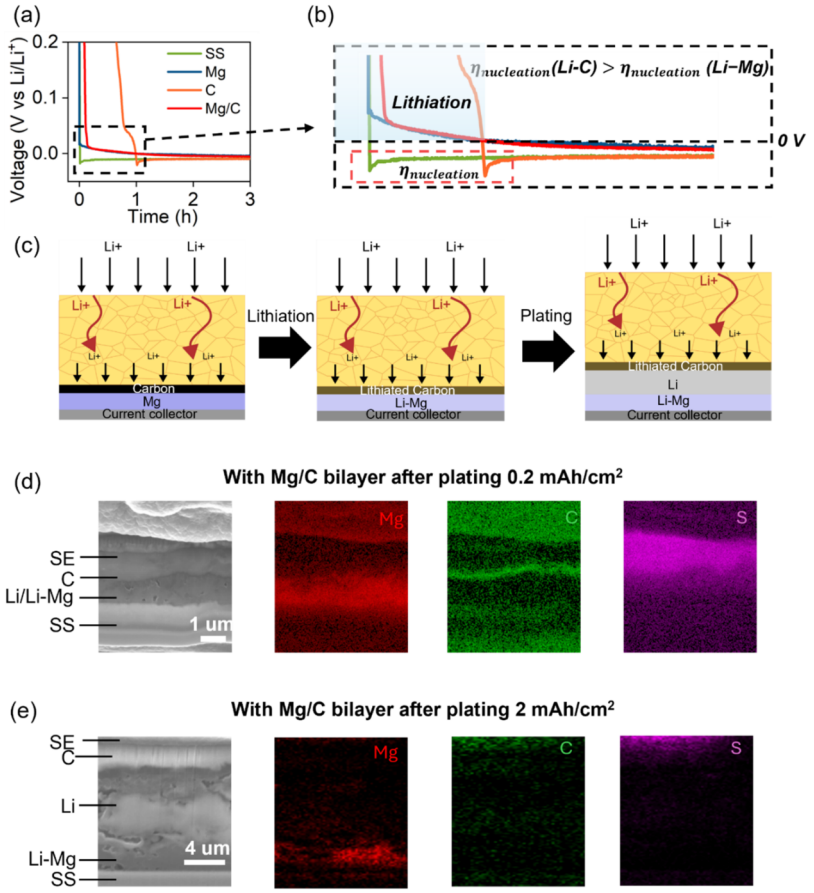

Figure 2. (a) Voltage profiles of the initial 0.3 mAh/cm^2 plating during the first plating on various current collectors. (b) Comparison of the overpotential for Li plating for various current collectors. (c) Schematic showing the mechanism of regulating Li plating by Mg/C bilayer. (d, e) Cross-sectional FIB/SEM image and EDS mapping of the SS|Mg/C|LPSC|Li−In cell after plating 0.2 mAh/cm^2 (d, e) 2 mAh/cm^2.

why not separate them at the beginning? In this case, we can ensure that on the top surface of a Ag−C nanocomposite interlayer, there will be no Ag particles that lead to Li plating on top of C to affect the separation of SE with plated Li. We kept carbon on the top layer to separate the SE from the plated Li because its softness can maintain a good interfacial contact, which is relatively hard to achieve for a metal such as W.[36] We replaced Ag with a low-cost metal, Mg, because Mg has a very similar property to Ag, i.e., high intersolubility without the presence of any intermediate phase when compared with other metals such as Zn and Sn.[33] Moreover, separating Mg and C into two layers allows us to independently study the role of each layer in regulating Li plating, which enabled us to develop novel understandings of the working principles of the metal−carbon interlayer.

RESULTS AND DISCUSSION

The bilayer was fabricated by thermal evaporation of Mg and C sequentially on a 10 μm-thick stainless-steel (SS) current collector. Mg and C_{60} were used as targets for the deposition. Figure 1(a) shows the cross-sectional SEM image and EDS line scan of the Mg/C bilayer. The thicknesses of Mg and C are around 500 and 100 nm, respectively. Figure 1(b) presents the surface morphology of the prepared Mg/C bilayer by atomic force microscope (AFM). The image shows a smooth surface with a roughness of around 84.12 pm. The surface roughness is close to that of evaporated Mg (Figure S1), indicative of a uniform coating of carbon on the Mg surface. The AFM image also suggests that the grain size of evaporated Mg is relatively uniform. The XRD pattern of the Mg/C bilayer (Figure 1(c)) suggests that the evaporated Mg has a hexagonal close-packed (hcp) structure with a preferential orientation of (0001).[37] No apparent diffraction of carbon can be observed.[38] X-ray photoelectron spectroscopy and Raman spectroscopy were used to study the surface chemistry of carbon. The C 1s XPS spectra (Figure 1(d)) show coexistence of sp^2 carbon (284.0 eV), sp^3 carbon (285.0 eV), and C−O bond (286.4 eV). The Raman spectrum (Figure 1(e)) shows typical features of a C_{60} film with three peaks at 494, 771, and 1467 cm^{-1}, corresponding to the $A_g(1)$, $H_g(4)$, and $A_g(2)$[39] vibrations, respectively, with a shoulder peak in the 1560−1620 cm^{-1} due to the existence of amorphous carbon.[40]

The Mg/C bilayer was integrated into a solid-state cell using lithium argyrodite Li_6PS_5Cl (LPSC) as the SE and the $Li_{0.5}In$ (Li−In) alloy as the cathode. Li−In was used as the counter and reference electrode because of its excellent stability with LPSC and its stable voltage plateau (~0.62 V vs Li/Li$^+$) during alloying and dealloying.[41] A constant current of 0.1 mA/cm^2 was used for plating and stripping at room temperature. The areal capacity for the initial plating is set to be 2 mAh/cm^2, and the cutoff voltage for stripping is 1.5 V vs Li/Li$^+$. Figure 2a,2b shows the voltage profile of the initial 0.3 mAh/cm^2 plating during the first plating of the anode-free cells with various current collectors. We also prepared single-layer Mg and C films in the same way as the Mg/C bilayer to separately study their effects on Li plating/stripping. Apparent capacities can be

https://doi.org/10.1021/acsami.6c01094
ACS Appl. Mater. Interfaces XXXX, XXX, XXX−XXX

seen above 0 V vs Li/Li$^+$, suggesting the lithiation processes for Mg, C, and Mg/C bilayers. Lithiation of carbon occurs at a much higher potential, consistent with the charge/discharge curve of C_{60}-based anodes.[42] Lithiation of the carbon interlayer was also reported in a previous report.[43,44] A larger lithiation capacity can be observed for the Mg/C bilayer than for Mg. A distinct voltage minimum, indicative of the overpotential for Li nucleation, can be observed for cells with SS and C current collectors, but not for the cells with Mg and Mg/C. The existence of a nucleation overpotential on lithiated carbon (Li−C) was also reported in a previous work.[45] The large differences in the nucleation overpotential suggest that Li tends to nucleate on Li−Mg rather than Li−C. As a result, when a Mg/C bilayer was used, Li would be plated at the interface between Li−C and Li−Mg rather than at the interface between Li−C and the SE, as demonstrated in the schematic in Figure 2c. The results were also validated from the cross-sectional SEM image and elemental mapping of the cell with the Mg/C bilayer after plating at 0.2 mAh/cm^2 (Figure 2d) and 2 mAh/cm^2 capacity (Figures 2e and S2). In both cases, Li was plated underneath the carbon. Alloying of Mg was also observed from the increase in the thickness of the Mg-containing layer from 500 nm to 2 μm. Different from the cell with the bare SS current collector (Figure S3), no apparent delamination at the interfaces with the SE and current collector can be observed for the cell with the Mg/C interlayer. Similar surface morphologies can also be observed for Mg/C after stripping (Figure S4). The results suggest that the utilization of the multifunctional Mg/C interlayer can lead to uniform and preferential plating of Li for anode-free solid-state cells.

To understand the effect of the interlayer on the plating-stripping kinetics, we also measured the EIS during plating-stripping with and without the Mg/C bilayer. Figure 3a shows the voltage profiles of the SS|LPSC|Li−In cell and the SS|Mg/C|LPSC|Li−In cell tested at 0.1 mA/cm^2. A larger stripping capacity can be observed for the cell with the Mg/C interlayer, suggesting an increase in the Coulombic efficiency. EIS was measured every two h during the plating and stripping test. For both cells, a change from blocking to nonblocking behavior can be observed for the Nyquist plots as soon as the plating started (Figure 3b,3d). At the end of stripping, a change of behavior from nonblocking to blocking can be observed (Figure 3c,e). We also extracted the anode/electrolyte interfacial resistances based on fitting the Nyquist plots (Figure S5), as shown in Figure 3(f). Apparent change can be observed for the anode/electrolyte interfacial resistance for the cell without an interlayer, with a general trend of first increasing to 45 Ω during plating and then decreasing during stripping. However, for the cell with a Mg/C bilayer, the interfacial resistance remains around 14 Ω. The results suggest that the introduction of the Mg/C bilayer can help maintain the interfacial stability between the anode and the SE.

To further understand the effects of Mg/C bilayer on the kinetics during plating and stripping, we calculated the distribution of relaxation time (DRT)[46] based on the measured Nyquist plots. Given that DRT analysis does not require an established model of discrete impedance contribution, the results can provide additional information to complement the EIS. Peaks in the DRT in specific time constant ranges can be interpreted to represent electrochemical processes within the cell since the time constant τ is defined as the product of characteristic resistance and capacitance ($\tau = RC$). The DRT in this work (Figure 4a,b,e,f) generally indicates four main

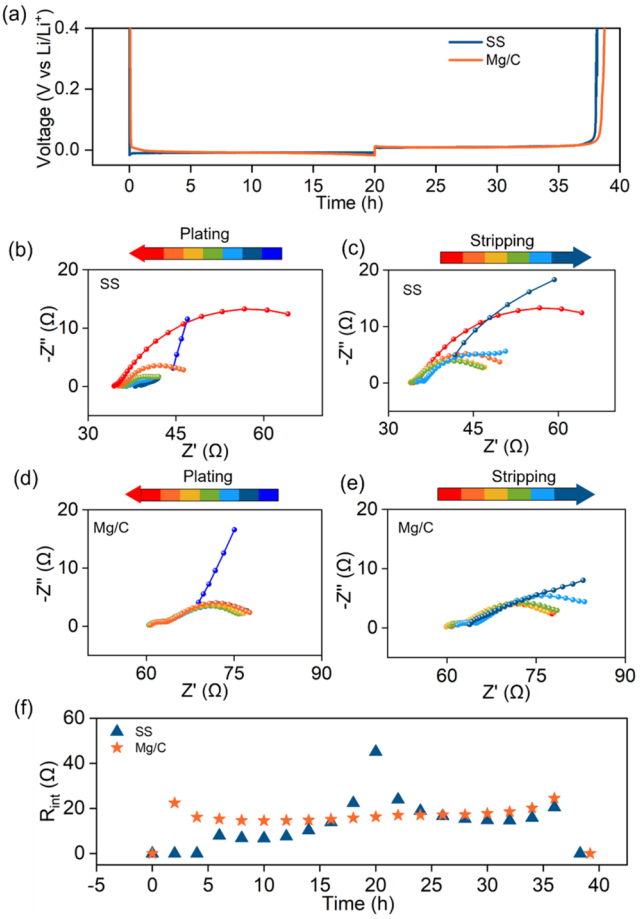

Figure 3. (a) Voltage profiles of the plating and stripping of the SS|LPSC|Li−In and SS|Mg/C|LPSC|Li−In cell. The cells were tested at 0.1 mA/cm^2 at room temperature with *a* charge cutoff voltage of 1.5 V vs Li/Li$^+$. Evolution of EIS during initial plating (b, d) and stripping (c, e) of the SS|LPSC|Li−In and the SS|Mg/C|LPSC|Li−In cells. EIS was measured in the frequency range of 1 MHz to 1 Hz with *a* perturbation voltage of 10 mV. (f) Evolutions of anode/electrolyte interfacial resistances during plating and stripping of the SS|LPSC|Li−In and SS|Mg/C|LPSC|Li−In cells.

peaks. Based on the DRT of SS/LPSC/SS and Li−In/LPSC/Li−In reference cells (Figure S6), the two peaks at the shorter time constant (P1 at $\tau = 10^{-6}$ s and P2 at $\tau = 10^{-5}$ s) represent the resistance for the ionic resistance in the solid electrolyte. The two peaks at longer time constant (P3 at $\tau = 10^{-2}$ and P4 at 1 s) relate to Li-ion transport through the anode (Li or Li−In)-electrolyte interphase(s) and charge transfer resistance of the Li or Li−In anode, respectively.[47] Given the excellent stability between Li−In and LPSC solid electrolyte, the evolution of the P3 and P4 can be mainly attributed to the interfacial process between Li and LPSC. Without the Mg/C bilayer, the 2D DRT surface shows a continuous increase in the P3 and P4 peaks during plating (Figure 4c), indicating a continuous increase in the anode/electrolyte resistances. Upon subsequent stripping, those two peaks first decrease and then increase. A slight increase in the solid electrolyte resistance of Li−In/LPSC can also be observed at the end of stripping (Figure 4d), suggesting possible effects of plating/stripping on the effective contact of the solid electrolyte. A similar trend can be observed for the cell with just Mg as the interlayer (Figure S7).

https://doi.org/10.1021/acsami.6c01094
ACS Appl. Mater. Interfaces XXXX, XXX, XXX−XXX

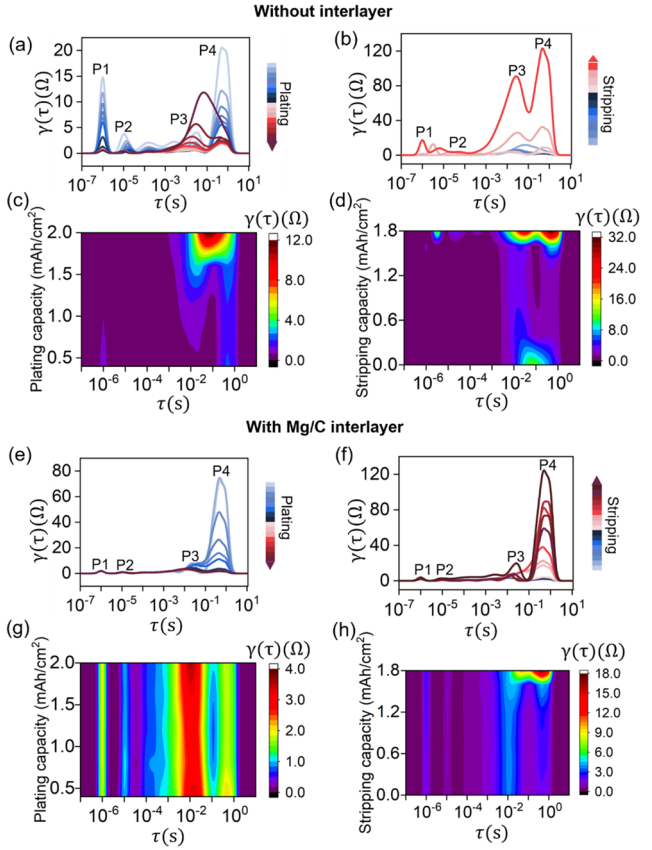

Figure 4. DRT evolution (a, b) and corresponding 2D DRT surface (c, d) during plating and stripping of the SS|LPSC|Li−In cell. DRT evolution (e, f) and corresponding 2D DRT surface (g, h) during plating and stripping of the SS|Mg/C|LPSC|Li−In cell.

We believe that the impedance evolution is strongly related to the morphological change of Li during plating and stripping. Without the interlayer, Li will plate nonuniformly (Figure S3), and the formation of Li islands will lead to contact loss with the SE and SS current collectors, leading to an increase in the anode/electrolyte resistances. During stripping, Li on the tip will be first stripped due to better kinetics. The process will lead to a slight improvement in the interfacial contact, reducing the anode/electrolyte resistances. However, since the stripping occurs nonuniformly, further stripping will lead to the formation of voids and pores at the interfaces, thus increasing the impedance. The volume change during plating and stripping can be so large that under fixed stack pressure (15 MPa in this study), the interfacial contact between the electrode and SE was also affected. On the other hand, with the Mg/C bilayer, the interfacial resistance and charge transfer resistance of the anode are much smaller (Figure 4g,4h). More importantly, they remain relatively stable during plating and stripping with no apparent effects on solid electrolyte resistance (Figure 4g,4h) due to more uniform plating and stripping (Figure 2d,2e). Note that the increase in the P4 peak at the end of stripping is mainly attributed to the sharp increase from nonblocking to blocking behavior.

Figure 5a,5b shows the voltage profiles during galvanostatic cycling of the SS|LPSC|Li−In and SS|Mg/C|LPSC|Li−In half cells. The initial Coulombic efficiency increases from 90.9% to 96.1% after introducing the Mg/C bilayer. The initial Coulombic efficiency of SS|Mg/C|LPSC|Li−In is much higher than that of the cells with Mg as the interlayer (94.2%, Figure S8) and with Cu as the current collector (92.7%, Figure S9). Without the interlayer, the Coulombic efficiency quickly decreases for the first few cycles (Figure 5a). Voltage spikes can also be observed from the profile starting from the third cycle, possibly due to soft shorting of the cell. Stable plating/

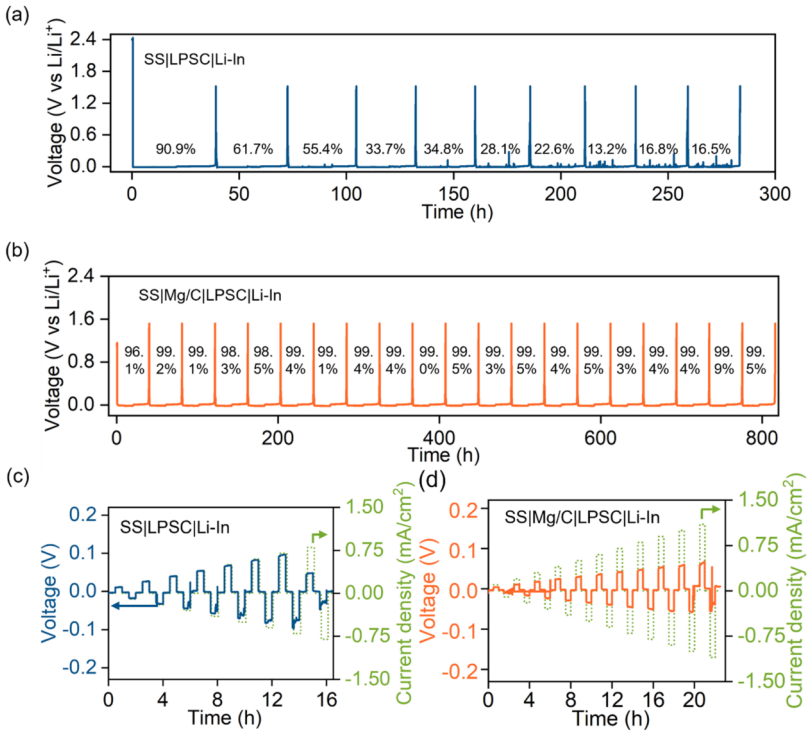

Figure 5. Galvanostatic cycling of SS|LPSC|Li−In (a) and SS|Mg/C|LPSC|Li−In (b) at 0.1 mA/cm^2 with a plating/stripping capacity of 2 mAh/cm^2. Critical current densities of SS|LPSC|Li−In (c) and SS|Mg/C|LPSC|Li−In (d) at 0.1 mA/cm^2. All tests were performed at room temperature.

https://doi.org/10.1021/acsami.6c01094
ACS Appl. Mater. Interfaces XXXX, XXX, XXX−XXX

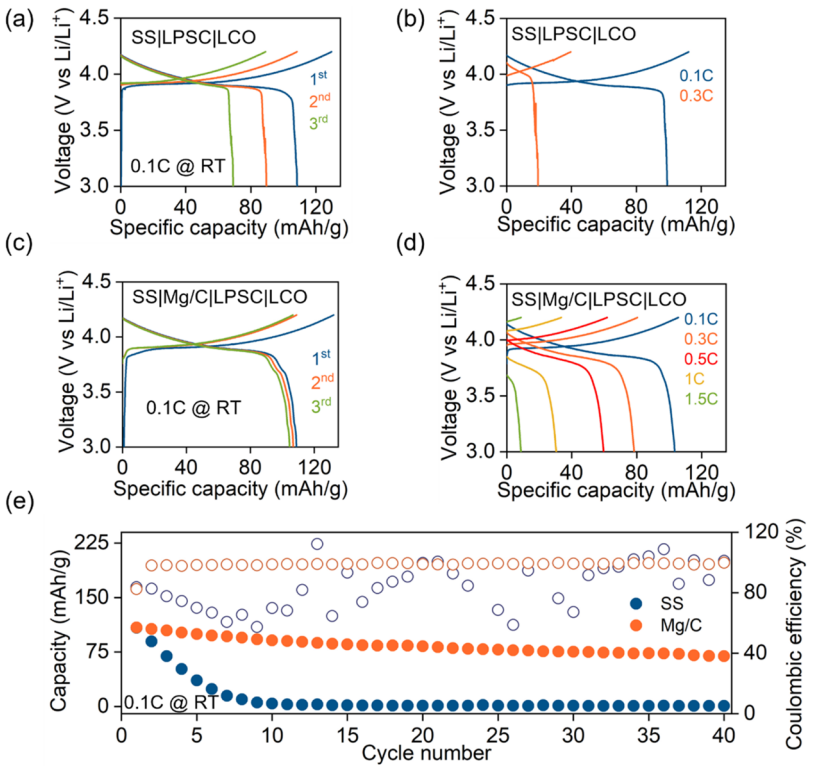

Figure 6. Electrochemical performance of anode-free solid-state full cells. Charge/discharge curves of the SS|LPSC|LCO cell (a) and the SS|Mg/C|LPSC|LCO cell (c) for the first three cycles at 0.1C. Rate performances of the SS|LPSC|LCO cell (b) and the SS|Mg/C|LPSC|LCO cell (d). (e) Cycling performance of SS|LPSC|LCO and SS|Mg/C|LPSC|LCO cells at 0.1C. All tests were performed at room temperature.

stripping cycles can be observed with the Mg/C bilayer (Figure 5b) with an average columbic efficiency of >99%. Furthermore, the SS|Mg/C|LPSC|Li−In cell can also achieve a 92.1% initial Coulombic efficiency at 0.5 mAh/cm^2 with a 2 mAh/cm^2 plating/stripping capacity (Figure S10). The cycling stability of the Mg/C bilayer is also much better than that of the Mg interlayer (Figure S8) and Cu (Figure S9). To investigate the effect of the interlayer on dendrite suppression, we also tested the critical current density (CCD), where the cell shorts occur because of dendrite penetration, of the cells with and without the interlayer. The test was performed by plating 3 mAh/cm^2 of Li on the current collector, followed by gradually increasing the current density for the plating/stripping test (Figure 5c,d). A large increase in the critical current density from 0.3 to 1.1 mA/cm^2 at room temperature can be obtained with the interlayer. The results suggest that the uniform deposition and dissolution of Li due to the Mg/C bilayer helps to improve the cycling stability and dendrite suppression capability at various current densities of the solid-state cells.

To further validate the performance of the Mg/C bilayer, we also fabricated all-solid-state anode-free cells with $LiCoO_2$ (LCO) as the cathode.

Figure 6a,6c shows the charge−discharge curves of solid-state anode-free full cells with and without the Mg/C bilayer. Typical charge/discharge profiles of the LCO cathode can be observed for both cells. A slight slope at voltages lower than 3.9 V vs Li/Li$^+$ can be observed for the first charging process of the cell with the Mg/C bilayer, and this is attributed to the lithiation of Mg and C in the interlayer, which occurs at a higher potential than Li plating. The charge/discharge capacities for the first cycle are 129.6/108.4 mAh/g for the SS|LPSC|LCO cell and 132.1/108.8 mAh/g for the SS|Mg/C|LPSC|LCO cell, corresponding to the initial Coulombic efficiency of 83.7% and 82.4%, respectively. The Coulombic efficiency of the SS|Mg/C|LPSC|LCO cell increases to 98.0% for the second cycle and to 98.1% for the third cycle, while they remain low (82.7% for the second cycle and 77.7% for the third cycle) for the SS|LPSC|LCO cell. The anode-free cell with the Mg/C bilayer also demonstrated a much better cycling performance with a higher Coulombic efficiency over long-term cycling (Figure 6e). Figure 6b,6d shows the charge−discharge curve of the anode-free cells at higher rates. While the cell without an interlayer shorted at 0.3C, an anode-free cell with the Mg/C bilayer can be cycled at a much higher rate up to 1.5C. The results validate improved reversibility, stability, and dendrite suppression capability at a higher current after introducing the Mg/C bilayer.

The results suggest that due to the larger nucleation overpotential of Li−C than Li−Mg, Li will not plate on the Li−C; instead, it will penetrate through the Li−C and plate on the Li−Mg. In order to achieve this, the key requirement is that the energy barrier for the transport of Li through the Li−C has to be smaller than the difference in the nucleation overpotential on Li−C and Li−Mg ($\eta_{Li\text{-}C}-\eta_{Li\text{-}Mg}$). Because the nucleation of Li in between two solid layers involves the elimination of the interface between Li−C and Li−Mg, the creation of two new interfaces between Li nuclei and the two layers under stress, the overpotential for nucleation is a strong function of the properties of the materials such as the diffusivity, solubility, and interfacial chemistry of metals, as well as electronic conductivity, degree of graphitization, and surface chemistry of carbon, and also a function of interfacial mechanics, such as interfacial toughness.[48] In this regard, this work helps understand the working principle of metal−carbon

https://doi.org/10.1021/acsami.6c01094
ACS Appl. Mater. Interfaces XXXX, XXX, XXX−XXX

interlayers through insights that cannot be revealed from a metal−carbon nanocomposite interlayer because it is not possible to separately determine the nucleation overpotential of carbon and metal in a nanocomposite interlayer.[24] We suspect that the materials' properties will dominate overpotential, which explains why generally metals with higher intersolubility and diffusivity with Li work better because they tend to lead to a lower nucleation overpotential and why amorphous carbon works better than graphite because it tends to lead to a higher nucleation overpotential. However, under extreme mechanical conditions, interfacial mechanics may override the role of material properties, thus leading to inconsistent results from the literature. This explains that using a higher pressure to fabricate the cell does not necessarily improve the Li cycling performance due to changes in the interfacial mechanics (Figure S11). A continuum-level electro-chemo-mechanical modeling can be used to quantitatively determine the exact nucleation overpotential with two different layers under a certain interfacial toughness.[49] The quantitative understanding of the nucleation overpotential can also open a large design space for low-cost metal, interfacial architecture, and interlayer processing techniques. It should also be noted that the utilization of a metal/carbon bilayer structure does not necessarily reduce the overall kinetics for lithiation and nucleation/growth compared with a metal−carbon nanocomposite interlayer, as very similar capacity and rate performance can be observed for Ag/C bilayer and Ag−C nanocomposite interlayers.[26]

We would also like to note that, while metal−carbon interlayers have been used to enable stable Li cycling in anode-free solid-state cells, the Li transport mechanism in the lithiated carbon remains elusive.[25,50] It is still under intense debate whether Li ions or Li atoms are the major carriers for the transport of Li in the carbon-containing interlayers. Quantifying the diffusion coefficient of Li^+ and Li^0 and separating the surface and bulk transport would provide critical information for further development of metal−carbon interlayers for anode-free solid-state batteries. While C_{60} was used as the target for depositing the C interlayer, based on the available resource, we believe that many low-cost amorphous carbons such as carbon black and hard carbon[24,34,43] would have a similar role in the Mg/C bilayer. Another potential challenge of utilizing the Mg−C bilayer is the volume change of Mg after alloying, which can cause the interfacial delamination between Li/Li−Mg as well as Li−Mg/SS interfaces. Combining a carbon interlayer with a 3D Li−Mg host might help accommodate the volume change of the Li−Mg alloy and further improve its performance.

CONCLUSION

In summary, we developed an Mg/C bilayer interphase for anode-free solid-state batteries based on Li_6PS_5Cl SE. Both Mg and C will be lithiated at the beginning of the charging process. We observed a large overpotential for the nucleation of Li on Li−C vs Li−Mg, promoting Li deposition at the interface between Li−C/Li-Mg rather than SE/Li−C. Cross-sectional SEM and elemental mapping were also used to validate the regulated Li plating behavior. EIS analysis during plating-stripping suggests a much more stable interface after introducing the Mg/C bilayer. Due to the effective separation of SE and plated Li by Li−C, the Mg/C bilayer also enabled Li plating/stripping at a high current density. The uniform deposition/stripping as well as the excellent dendrite suppression capability enabled stable plating/stripping cycles of Mg/C bilayer with an areal capacity of 2 mAh/cm^2 and an averaged Coulombic efficiency of >99%. The excellent performance of the Mg/C bilayer also enabled an anode-free solid-state full cell with a $LiCoO_2$ cathode. Moreover, the findings also enabled us to propose our understanding of the working mechanism of various metal−carbon interlayers based on the nucleation overpotential, which is determined by both the materials' properties and the interfacial mechanics. We hope the findings can provide insights for the design of a low-cost, high-performance interlayer for anode-free solid-state batteries.

EXPERIMENTAL SECTION

Material Synthesis

Mg/C bilayer fabrication: a 10 μm-thick stainless-steel substrate was utilized as the substrate for the deposition of the Mg/C bilayer, and it was cleaned with acetone and ethanol and then dried at 80 °C overnight. Mg/C bilayer was prepared by using the thermal evaporation method. The thermal evaporation system (MBraun) is integrated into an Ar-filled glovebox (MBraun), and the H_2O and O_2 levels were kept under <0.1 ppm. The deposition process was controlled using a quartz crystal controller (Inficon GmbH) and a quartz microbalance crystal sensor. The stainless-steel current substrates were fixed on a rotating glass substrate, and the chamber was depressurized to 10−6 mbar. Stainless-steel source crucibles were used for both Mg and C_{60} deposition. Mg was first heated to reach a deposition rate of 5 Å/s, and a 500 nm-thick Mg layer was deposited. C_{60} was then deposited at a rate of 0.2 Å/s until a thickness of 100 nm was reached. Single-layer Mg and C_{60} films were also deposited by using the same protocol to separately study the effect of Mg and C on Li plating/stripping. The thicknesses of single-layer Mg and C60 films are 500 nm and 1 μm, respectively. Li−In anode was prepared by mixing lithium powder and indium powder (99.99%, Sigma-Aldrich) utilizing a vortex mixer (VX-200, VWR) for 30 min. The molar ratio of lithium powder and indium powder was 2:1. The $LiCoO_2$ cathode composite was prepared by mixing the coated $LiCoO_2$ and LPSC SE (NEI Corporation) at a weight ratio of 60:40 wt % at 100 rpm for 1 h using PM100 (Retsch, Germany). All of the experiments were performed in an argon glovebox (H_2O < 0.5 ppm, O_2 < 0.5 ppm).

Cell Fabrication

The half cells were prepared by placing 100 mg of LPSC SE into a polyether ether ketone (PEEK) mold (10 mm diameter) and pressing at 75 MPa for 2 min. Then, the current collector was attached to one side of the pellet, and 100 mg of Li−In powder was added to the other side of the pellet. Subsequently, 250 MPa was applied for 2 min. When assembling the full cells. 80 mg of LPSC SE was pressed in a PEEK mold at 75 MPa for 2 min. The current collector was attached to one side of the pellet, and then the composite cathode (5 mg) was uniformly dispersed on the other side of the SE and pressed at 350 MPa for 2 min. The external stacking pressure for all cells was 15 MPa.

Electrochemical Measurements

All galvanostatic cycling tests were performed on a LAND battery tester (Wuhan LAND Electronics Co., Ltd.). Electrochemical impedance spectroscopy (EIS) tests were performed

https://doi.org/10.1021/acsami.6c01094
ACS Appl. Mater. Interfaces XXXX, XXX, XXX−XXX

on a Biologic electrochemical station. The measurement frequency was 1 Hz to 1 MHz, and the amplitude was 10 mV. The EIS fitting was achieved by Z-View software. All of the electrochemical tests were conducted at room temperature. At least three cells were tested under each condition with error limits of <3%.

Material Characterization

Carl Zeiss 1540EsB Crossbeam was used for the SEM, FIB-SEM, and the EDS test. X-ray diffraction test was performed using a PanAlytical X'Pert Diffractometer with a copper irradiation source (Cu Ka 1/4 0.15406 nm). The Raman spectroscopy was conducted by a Renishaw Raman spectrometer with a 785 nm laser beam. PHI VersaProbe II XPS was used to record the XPS data. Asylum MFP3D AFM was used to investigate the surface morphology. The Amplitude Contrast (AC) mode was employed, and the scan area is 50 μm × 50 μm.

■ ASSOCIATED CONTENT

Supporting Information

The Supporting Information is available free of charge at https://pubs.acs.org/doi/10.1021/acsami.6c01094.

AFM altitude of Mg interlayer; cross-sectional FIB/SEM image and EDS line scan of the SS|Mg/C|LPSC|Li−In; cross-sectional FIB/SEM image and EDS mapping of the SS|LPSC|Li−In cell; EIS fitting model and fitting result; DRT analysis for the SS|LiPSC|SS cell, the Li−In|LiPSC|Li−In cell, and the SS|Mg||LPSC|Li−In cell; galvanostatic cycling of SS|Mg/C|LPSC|Li−In at 0.5 mA/cm^2 with a plating capacity of 2 mAh/cm^2; and cycling performance of SS|Mg||LPSC|Li−In cell, Cu|LPSC|Li−In cell, and Cu||LPSC|LCO cell (PDF)

■ AUTHOR INFORMATION

Corresponding Authors

Chengyin Fu − *Battery Innovation Hub, Centre Suisse d'Électronique et de Microtechnique (CSEM), Neuchâtel 2000, Switzerland*; Email: chengyin.fu@csem.ch

Fudong Han − *Battery Innovation Hub, Centre Suisse d'Électronique et de Microtechnique (CSEM), Neuchâtel 2000, Switzerland*; orcid.org/0000-0003-2507-4340; Email: hanf2@rpi.edu

Authors

Ruixin Wu − *Department of Mechanical, Aerospace and Nuclear Engineering, Rensselaer Polytechnic Institute, Troy, New York 12180, United States*

Sufu Liu − *Battery Innovation Hub, Centre Suisse d'Électronique et de Microtechnique (CSEM), Neuchâtel 2000, Switzerland*

Ruihao Deng − *Department of Mechanical, Aerospace and Nuclear Engineering, Rensselaer Polytechnic Institute, Troy, New York 12180, United States*

Ru Xiao − *Department of Mechanical, Aerospace and Nuclear Engineering, Rensselaer Polytechnic Institute, Troy, New York 12180, United States*

Keng Xu − *Department of Mechanical, Aerospace and Nuclear Engineering, Rensselaer Polytechnic Institute, Troy, New York 12180, United States*

Andrea Ingenito − *Battery Innovation Hub, Centre Suisse d'Électronique et de Microtechnique (CSEM), Neuchâtel 2000, Switzerland*

Complete contact information is available at: https://pubs.acs.org/10.1021/acsami.6c01094

Author Contributions

R.W. contributed to the experiments, characterizations, data analysis, and manuscript writing. S.L., C.F., and A.I. fabricated the Mg/C bilayer. R.D. contributed to material characterizations. R.X. and K.X. contributed to the data analysis. All authors discussed the results. F.H. supervised the project and edited the manuscript.

Notes

The authors declare no competing financial interest.

■ ACKNOWLEDGMENTS

The authors acknowledge support from the US National Science Foundation (Award No. DMR-2223217).

■ REFERENCES

(1) Krauskopf, T.; Richter, F. H.; Zeier, W. G.; Janek, J. Physicochemical Concepts of the Lithium Metal Anode in Solid-State Batteries. *Chem. Rev.* **2020**, *120* (15), 7745−7794.

(2) Liu, J.; Bao, Z.; Cui, Y.; Dufek, E. J.; Goodenough, J. B.; Khalifah, P.; Li, Q.; Liaw, B. Y.; Liu, P.; Manthiram, A.; et al. Pathways for Practical High-Energy Long-Cycling Lithium Metal Batteries. *Nat. Energy* **2019**, *4* (3), 180−186.

(3) Nanda, S.; Gupta, A.; Manthiram, A. Anode-Free Full Cells: A Pathway to High-Energy Density Lithium-Metal Batteries. *Adv. Energy Mater.* **2021**, *11* (2), No. 2000804.

(4) Qian, J.; Henderson, W. A.; Xu, W.; Bhattacharya, P.; Engelhard, M.; Borodin, O.; Zhang, J.-G. High Rate and Stable Cycling of Lithium Metal Anode. *Nat. Commun.* **2015**, *6* (1), No. 6362.

(5) Yan, K.; Lu, Z.; Lee, H.-W.; Xiong, F.; Hsu, P.-C.; Li, Y.; Zhao, J.; Chu, S.; Cui, Y. Selective Deposition and Stable Encapsulation of Lithium through Heterogeneous Seeded Growth. *Nat. Energy* **2016**, *1* (3), No. 16010.

(6) Qian, J.; Adams, B. D.; Zheng, J.; Xu, W.; Henderson, W. A.; Wang, J.; Bowden, M. E.; Xu, S.; Hu, J.; Zhang, J. Anode-Free Rechargeable Lithium Metal Batteries. *Adv. Funct. Mater.* **2016**, *26* (39), 7094−7102.

(7) Liang, P.; Sun, H.; Huang, C.; Zhu, G.; Tai, H.; Li, J.; Wang, F.; Wang, Y.; Huang, C.; Jiang, S.; et al. A Nonflammable High-Voltage 4.7 V Anode-Free Lithium Battery. *Adv. Mater.* **2022**, *34* (51), No. 2207361.

(8) Weber, R.; Genovese, M.; Louli, A. J.; Hames, S.; Martin, C.; Hill, I. G.; Dahn, J. R. Long Cycle Life and Dendrite-Free Lithium Morphology in Anode-Free Lithium Pouch Cells Enabled by a Dual-Salt Liquid Electrolyte. *Nat. Energy* **2019**, *4* (8), 683−689.

(9) Wang, M. J.; Carmona, E.; Gupta, A.; Albertus, P.; Sakamoto, J. Enabling "Lithium-Free" Manufacturing of Pure Lithium Metal Solid-State Batteries through in Situ Plating. *Nat. Commun.* **2020**, *11* (1), No. 5201.

(10) Jeon, S.; Kim, U.; Kwag, S. H.; Min, J.; Kim, D.; Kim, H.; Lee, Y.; Jung, Y. All-Solid-State Batteries with Anodeless Electrodes: Research Trend and Future Perspective. *Adv. Mater. Interfaces* **2025**, *12* (13), No. 2400953.

(11) Han, F.; Zhu, Y.; He, X.; Mo, Y.; Wang, C. Electrochemical Stability of Li_{10} GeP_2 S_{12} and Li_7 La_3 Zr_2 O_{12} Solid Electrolytes. *Adv. Energy Mater.* **2016**, *6* (8), No. 1501590.

(12) Luntz, A. C.; Voss, J.; Reuter, K. Interfacial Challenges in Solid-State Li Ion Batteries. *J. Phys. Chem. Lett.* **2015**, *6* (22), 4599−4604.

(13) Neudecker, B. J.; Dudney, N. J.; Bates, J. B. "Lithium-Free" Thin-Film Battery with In Situ Plated Li Anode. *J. Electrochem. Soc.* **2000**, *147* (2), No. 517.

(14) Sandoval, S. E.; Haslam, C. G.; Vishnugopi, B. S.; Liao, D. W.; Yoon, J. S.; Park, S. H.; Wang, Y.; Mitlin, D.; Hatzell, K. B.; Siegel, D. J.; et al. Electro-Chemo-Mechanics of Anode-Free Solid-State Batteries. *Nat. Mater.* **2025**, *24* (5), 673−681.
(15) Han, F.; Westover, A. S.; Yue, J.; Fan, X.; Wang, F.; Chi, M.; Leonard, D. N.; Dudney, N. J.; Wang, H.; Wang, C. High Electronic Conductivity as the Origin of Lithium Dendrite Formation within Solid Electrolytes. *Nat. Energy* **2019**, *4* (3), 187−196.
(16) Hatzell, K. B.; Chen, X. C.; Cobb, C. L.; Dasgupta, N. P.; Dixit, M. B.; Marbella, L. E.; McDowell, M. T.; Mukherjee, P. P.; Verma, A.; Viswanathan, V.; et al. Challenges in Lithium Metal Anodes for Solid-State Batteries. *ACS Energy Lett.* **2020**, *5* (3), 922−934.
(17) Sun, C.; Li, Y.; Sun, Z.; Yuan, X.; Jin, H.; Zhao, Y. Ferroelectric Interface for Efficient Sodium Metal Cycling in Anode-Free Solid-State Batteries. *Mater. Today* **2024**, *80*, 395−405.
(18) Lee, N.; Oh, J.; Choi, J. W. Anode-Less All-Solid-State Batteries: Recent Advances and Future Outlook. *Mater. Futures* **2023**, *2* (1), No. 013502.
(19) Kasemchainan, J.; Zekoll, S.; Jolly, D. S.; Ning, Z.; Hartley, G. O.; Marrow, J.; Bruce, P. G. Critical Stripping Current Leads to Dendrite Formation on Plating in Lithium Anode Solid Electrolyte Cells. *Nat. Mater.* **2019**, *18* (10), 1105−1111.
(20) Lewis, J. A.; Sandoval, S. E.; Liu, Y.; Nelson, D. L.; Yoon, S. G.; Wang, R.; Zhao, Y.; Tian, M.; Shevchenko, P.; Martínez-Pañeda, E.; Martínez-Pañeda, E. Accelerated Short Circuiting in Anode-Free Solid-State Batteries Driven by Local Lithium Depletion. *Adv. Energy Mater.* **2023**, *13* (12), No. 2204186.
(21) Haslam, C. G.; Fuchs, T.; Liao, D. W.; Becker, J.; Dasgupta, N. P.; Janek, J.; Sakamoto, J. The Effect of Alloying Interlayers on Lithium Anode Morphology and Microstructure in "Anode-Free" Solid-State Batteries. *ACS Energy Lett.* **2025**, *10* (5), 2285−2291.
(22) Sandoval, S. E.; Lewis, J. A.; Vishnugopi, B. S.; Nelson, D. L.; Schneider, M. M.; Cortes, F. J. Q.; Matthews, C. M.; Watt, J.; Tian, M.; Shevchenko, P.; Mukherjee, P. P.; McDowell, M. T. Structural and Electrochemical Evolution of Alloy Interfacial Layers in Anode-Free Solid-State Batteries. *Joule* **2023**, *7* (9), 2054−2073.
(23) Huang, Y.; Zhang, Y.; Wu, R.; Shao, B.; Deng, R.; Das, R.; Han, F. Hydride-Based Interlayer for Solid-State Anode-Free Battery. *ACS Energy Lett.* **2024**, *9* (7), 3409−3417.
(24) Lee, Y.-G.; Fujiki, S.; Jung, C.; Suzuki, N.; Yashiro, N.; Omoda, R.; Ko, D.-S.; Shiratsuchi, T.; Sugimoto, T.; Ryu, S.; et al. High-Energy Long-Cycling All-Solid-State Lithium Metal Batteries Enabled by Silver−Carbon Composite Anodes. *Nat. Energy* **2020**, *5* (4), 299−308.
(25) Fuchs, T.; Aktekin, B.; Hartmann, F.; Burkhardt, S.; Janek, J. Lithium Batteries − Lithium Secondary Batteries − Lithium All-Solid State Battery | Negative Electrodes - "Anode Free. In *Encyclopedia of Electrochemical Power Sources*, 2nd ed.; Elsevier, 2025; pp 588−599 DOI: 10.1016/B978-0-323-96022-9.00169-9.
(26) Suzuki, N.; Yashiro, N.; Fujiki, S.; Omoda, R.; Shiratsuchi, T.; Watanabe, T.; Aihara, Y. Highly Cyclable All-Solid-State Battery with Deposition-Type Lithium Metal Anode Based on Thin Carbon Black Layer. *Adv. Energy Sustainability Res.* **2021**, *2* (11), No. 2100066.
(27) Jun, D.; Jung, J. E.; Yim, H.; Kim, H.; Lee, S. G.; Kim, K. S.; Shim, S.; Kim, T. E.; Lee, Y. J. Solubility Does Not Matter: Engineered Anode Architectures Activates Cost-Effective Metals for Controlled Lithium Morphology in Li-Free all-Solid-State Batteries. *Adv. Energy Mater.* **2025**, *15*, No. e02956.
(28) Park, S. H.; Jun, D.; Jung, J. E.; Lee, S. G.; Lee, G. H.; Lee, Y. J. Clarification of Li Deposition Behavior on Anodes with a Porous Interlayer in Li-Free All-Solid-State Batteries. *J. Mater. Chem. A* **2022**, *10* (41), 21995−22006.
(29) Chen, Y.; Wang, Z.; Li, X.; Yao, X.; Wang, C.; Li, Y.; Xue, W.; Yu, D.; Kim, S. Y.; Yang, F.; et al. Li Metal Deposition and Stripping in a Solid-State Battery via Coble Creep. *Nature* **2020**, *578* (7794), 251−255.
(30) Park, S. H.; Jun, D.; Lee, G. H.; Lee, S. G.; Jung, J. E.; Bae, K. Y.; Son, S.; Lee, Y. J. Designing 3D Anode Based on Pore-Size-Dependent Li Deposition Behavior for Reversible Li-Free All-Solid-State Batteries. *Adv. Sci.* **2022**, *9* (28), No. 2203130.
(31) Wu, C.; Emley, B.; Zhao, L.; Liang, Y.; Ai, Q.; Chen, Z.; Hernández, F. C. R.; Wang, F.; Risa, S.; Guo, H.; et al. Understanding the Chemomechanical Function of the Silver−Carbon Interlayer in Sheet-Type All-Solid-State Lithium−Metal Batteries. *Nano Lett.* **2023**, *23* (10), 4415−4422.
(32) Shozib, I. A.; Cúñez, F. D.; Ganter, M.; Leggiero, A.; Liu, R.; Tu, Q. H. Interplay of Interfacial Adhesion and Mechanical Degradation in Anode-Free Solid-State Batteries. *J. Electrochem. Soc.* **2024**, *171* (9), No. 090524.
(33) Xie, F.; Diallo, M. S.; Kim, H.; Tu, Q. H.; Ceder, G. The Microscopic Mechanism of Lithiation and Delithiation in the Ag/C Buffer Layer for Anode-Free Solid-State Batteries. *Adv. Energy Mater.* **2024**, *14* (10), No. 2302960.
(34) Liao, D. W.; Zeng, D.; Mulla, M.; Madanchi, A.; Kawakami, H.; Aihara, Y.; Aotani, K.; Thouless, M. D.; Dasgupta, N. P. Effects of Interfacial Adhesion on Lithium Plating Location in Solid-State Batteries with Carbon Interlayers. *Adv. Mater.* **2025**, *37*, No. 2502114.
(35) Avvaru, V. S.; Ogunfunmi, T.; Jeong, S.; Diallo, M. S.; Watt, J.; Scott, M. C.; Kim, H. Tin−Carbon Dual Buffer Layer to Suppress Lithium Dendrite Growth in All-Solid-State Batteries. *ACS Nano* **2025**, *19* (18), 17347−17356.
(36) Oh, J.; Choi, S. H.; Kim, H.; Kim, J. Y.; Lee, G.-J.; Bae, K. Y.; Lee, T.; Lee, N.; Sohn, Y.; Chung, W. J.; Choi, J. W. Lithio-Amphiphilic Nanobilayer for High Energy Density Anode-Less All-Solid-State Batteries Operating under Low Stack Pressure. *Energy Environ. Sci.* **2024**, *17* (20), 7932−7943.
(37) Ouyang, L.; Tang, J.; Zhao, Y.; Wang, H.; Yao, X.; Liu, J.; Zou, J.; Zhu, M. Express Penetration of Hydrogen on Mg($10\bar{1}3$) along the Close-Packed-Planes. *Sci. Rep.* **2015**, *5* (1), No. 10776.
(38) Itoh, T.; Nitta, S.; Nonomura, S. X-Ray Diffraction Patterns of C60 Films by the Thin Film Method and the Intercalation of O2. *Appl. Surf. Sci.* **1997**, *113−114*, 282−285.
(39) Kopova, I.; Bacakova, L.; Lavrentiev, V.; Vacik, J. Growth and Potential Damage of Human Bone-Derived Cells on Fresh and Aged Fullerene C60 Films. *Int. J. Mol. Sci.* **2013**, *14* (5), 9182−9204.
(40) Khalid, F. A.; Beffort, O.; Klotz, U. E.; Keller, B. A.; Gasser, P.; Vaucher, S. Study of Microstructure and Interfaces in an Aluminium−C60 Composite Material. *Acta Mater.* **2003**, *51* (15), 4575−4582.
(41) Wang, Y.; Liu, T.; Kumar, J. Effect of Pressure on Lithium Metal Deposition and Stripping against Sulfide-Based Solid Electrolytes. *ACS Appl. Mater. Interfaces* **2020**, *12* (31), 34771−34776.
(42) Yin, L.; Cho, J.; Kim, S. J.; Jeon, I.; Jeon, I.; Park, M.; Park, M.; Jeong, S.; Lee, D. H.; Seo, D.; Cho, C. Abnormally High-Lithium Storage in Pure Crystalline C_{60} Nanoparticles. *Adv. Mater.* **2021**, *33* (43), No. 2104763.
(43) Liao, D. W.; Cho, T. H.; Sarna, S.; Jangid, M. K.; Kawakami, H.; Kotaka, T.; Aotani, K.; Dasgupta, N. P. Interfacial Dynamics of Carbon Interlayers in Anode-Free Solid-State Batteries. *J. Mater. Chem. A* **2024**, *12* (10), 5990−6003.
(44) Hiraoka, K.; Sakabe, J.; Suzuki, N.; Seki, S. *Operando* and *Ex Situ* Raman Spectroscopies for Evaluating Carbon Structural Changes in Anode-Free-Type Sulfide-Based All-Solid-State Li-Ion Batteries. *J. Mater. Chem. A* **2025**, *13* (34), 27960−27969.
(45) Müller, A.; Paravicini, L.; Morzy, J.; Krause, M.; Casella, J.; Osenciat, N.; Futscher, M. H.; Romanyuk, Y. E. Influence of Au, Pt, and C Seed Layers on Lithium Nucleation Dynamics for Anode-Free Solid-State Batteries. *ACS Appl. Mater. Interfaces* **2024**, *16* (1), 695−703.
(46) Wan, T. H.; Saccoccio, M.; Chen, C.; Ciucci, F. Influence of the Discretization Methods on the Distribution of Relaxation Times Deconvolution: Implementing Radial Basis Functions with DRTtools. *Electrochim. Acta* **2015**, *184*, 483−499.
(47) Koerver, R.; Aygün, I.; Leichtweiß, T.; Dietrich, C.; Zhang, W.; Binder, J. O.; Hartmann, P.; Zeier, W. G.; Janek, J. Capacity Fade in Solid-State Batteries: Interphase Formation and Chemomechanical Processes in Nickel-Rich Layered Oxide Cathodes and Lithium

https://doi.org/10.1021/acsami.6c01094
ACS Appl. Mater. Interfaces XXXX, XXX, XXX−XXX

Thiophosphate Solid Electrolytes. *Chem. Mater.* **2017**, *29* (13), 5574−5582.
(48) Yang, S.; Li, C.; Zhang, Q.; Xin, L.; Li, L.; Wang, S.; Zhou, Q.; Wang, Z. Li Nucleation in Anode-Free Solid-State Batteries: The Role of Interfacial Mechanics. *J. Power Sources* **2025**, *644*, No. 237130.
(49) Raj, R.; Wolfenstine, J. Current Limit Diagrams for Dendrite Formation in Solid-State Electrolytes for Li-Ion Batteries. *J. Power Sources* **2017**, *343*, 119−126.
(50) Fuchs, T.; Haslam, C. G.; Moy, A. C.; Lerch, C.; Krauskopf, T.; Sakamoto, J.; Richter, F. H.; Janek, J. Increasing the Pressure-Free Stripping Capacity of the Lithium Metal Anode in Solid-State Batteries by Carbon Nanotubes. *Adv. Energy Mater.* **2022**, *12* (26), No. 2201125.

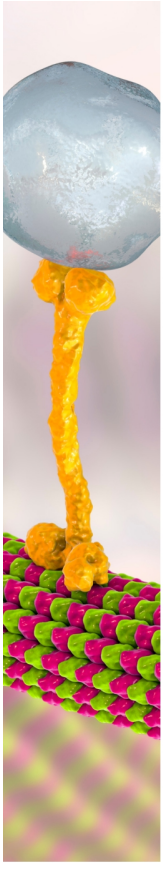
CAS BIOFINDER DISCOVERY PLATFORM™
BRIDGE BIOLOGY AND CHEMISTRY FOR FASTER ANSWERS
Analyze target relationships, compound effects, and disease pathways
Explore the platform
CAS
A division of the American Chemical Society

https://doi.org/10.1021/acsami.6c01094
ACS Appl. Mater. Interfaces XXXX, XXX, XXX−XXX